Spring 5-6-2016

Microstructure and Rheology of Carbon Nanotubes at Air-Water Interfaces

Charles D. Young
University of Connecticut - Storrs, charles.young@uconn.edu

Microstructure and Rheology of Carbon Nanotubes at Air-Water Interfaces

Charles Young
University of Connecticut
Honors Scholar Thesis
May 6, 2016

Chemical & Biomolecular Engineering Department
School of Engineering

Thesis Advisor – Anson Ma

Contents

1. Acknowledgements

First and foremost I would like to thank Professor Anson Ma and Sahil Vora, my faculty advisor and graduate mentor for almost 3 years now at UConn. I have learned a great deal and more from them regarding research procedures, the field of rheology and interfacial science, technical writing, and more. I will be pursuing a PhD in chemical engineering at the University of Illinois at Urbana Champaign this fall, and I attribute much of my progress to my advisors. I would also like to thank my family and friends for supporting and engaging me throughout me educational experience. Lastly I would like to thank the University of Connecticut for providing an affordable education with the help of a generous scholarship.

2. Abstract

This work characterizes the material properties of carbon nanotubes at air-water interfaces for potential use in creating stable emulsions. Properties such as length, aspect ratio, contact angle, microstructural ordering, surface pressure, compression and shear elastic moduli, stresses, surface viscosities and non-linearity are explored. Challenges such as deviation from a classical analysis of monolayers are encountered in the form of aggregation, mechanical contributions, and interface relaxation. These factors are taken into account to explain experimental measurements and trends. Ultimately, existing models for more homogeneous systems are resolved with observations to offer insight and areas of promise moving forward.

3. Introduction

3.1 Motivation

The adsorption of solid particles at liquid-liquid and gas-liquid interfaces was first observed more than a century ago [1] [2]. This effect causes interfacial films to form around droplets or bubbles of a dispersed substance, which protects them from coalescing into a separate phase. Such materials, where gases or liquids are suspended in a continuous liquid phase in which they are normally immiscible, are called foams (gas/liquid) or emulsions (liquid/liquid) [3]. Solid particle-stabilized emulsions are named Pickering emulsions after S. Pickering, who observed the effect in 1907 [2], although it should be noted that it was first discovered by Ramsden in 1903 [1].

Recent developments in methods for designing nanoparticles [4] [5] have renewed interest in the field due to advanced properties of such materials. In particular, graphene oxide and carbon nanotubes (CNTs) have been identified due to their potential in applications such as enhanced oil recovery [6] [7], oil spill cleanups [8] [9], poly-foams [10], and photocatalysis [11]. Additionally, the measurement of compression and shear viscoelasticity, the properties generally recognized as controlling particle adsorption, has become easier with the availability of Langmuir troughs and bi-cone or du Noüy ring rheometers [12] [13].

3.2 Background

To understand why Pickering emulsions occur, it is first necessary to consider the surface tension, denoted γ_{LG} with units of force per length, which causes droplets or bubbles to form and attract each other. A common example is the formation of water droplets on solid surfaces. From thermodynamics, water molecules will tends toward the lowest energy state. This state is determined from a balance on the adhesive and cohesive forces. Adhesive forces between the water and solid molecules cause the drop to spread across the surface, whereas cohesive forces between water molecules within the droplet cause avoid contact with the solid by balling up. Water molecules at the air-water interface experience minimal interaction with the air, and so feel only

inward acting forces, as seen in **Figure 1**.

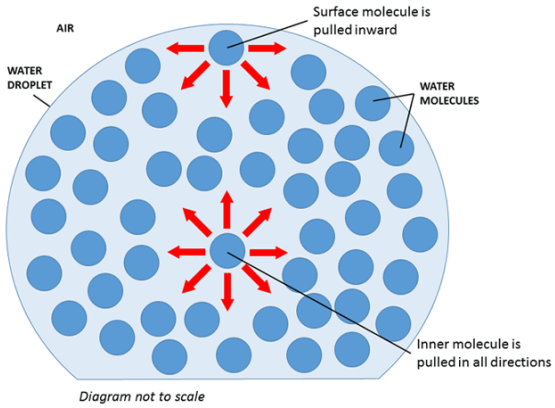

Figure 1 *– Diagram displaying forces on water molecules that cause surface tension [14]*

As a result, the droplet adopts a shape somewhere between a sphere and a film depending upon the affinity of water to the solid. Materials which are attracted to water are called hydrophilic, whereas those that are repelled are called hydrophobic. If the solid surface is completely hydrophobic, the shape of the droplet will become spherical because the dominant force becomes the pull of molecules at the interface towards inner molecules. A minimum is experienced where the ratio of surface area to volume is lowest (spherical shape), allowing the interfacial molecules to maximize interaction with interior ones, thereby lowering the energy of the droplet. The ability of a liquid to maintain contact with a solid surface as a result of intermolecular forces is called wetting. It is quantified by the contact angle θ_C and the surface energies γ_{SL}, γ_{LG}, and γ_{SG} via Young's equation (Equation 1), which is derived from the fact that at equilibrium, the net force per unit length (surface tension or energy) acting along the boundary between the three phases must be equal to zero [15].

$$\gamma_{SG} - \gamma_{SL} - \gamma_{LG}\cos(\theta_C) = 0 \tag{1}$$

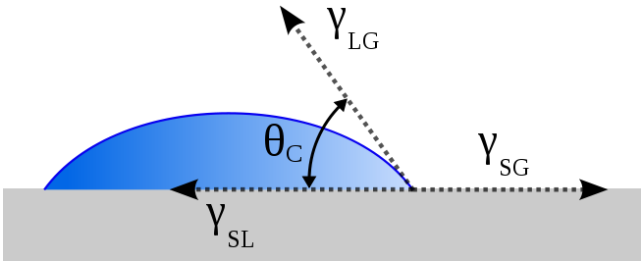

Figure 2 *– Diagram showing contact angle and interphase-energy between three phases [16]*

Extending this concept to many droplets in a liquid-liquid dispersion, such as oil in water, it is found that droplets coalesce when they collide [17], as observed in **Figure 3**. This is expected because it allows for droplets to further lower their surface tension. As time passes, the dispersed substance will phase separate to establish an equilibrium state.

The coalescence of droplets can be prevented, however, if the driving force of surface tension is reduced. Often this is achieved by use of a surfactant, an amphiphilic organic compound containing both hydrophobic and hydrophilic groups. The hydrophobic (lipophilic) parts are

usually called tails because they achieve their affinity to oil by long nonpolar hydrocarbon chains. The hydrophilic groups are often called heads because there are much smaller and polar. Surfactants reduce surface tension by adsorbing at the interface, thereby protecting the oil droplet, as seen in **Figure 4**. The oil-soluble tail resides in the dispersed phase while the water-soluble head forms a barrier around the droplet. These aggregates are called micelles.

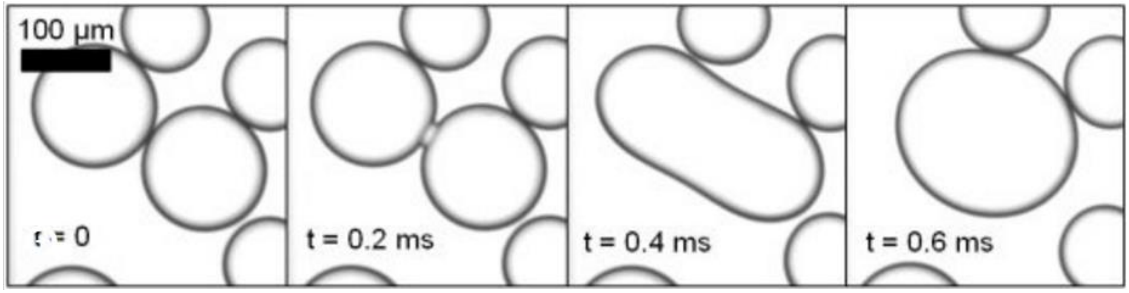

Figure 3 *– A series of images display coalescence between two pol droplets dispersed in oil [17]*

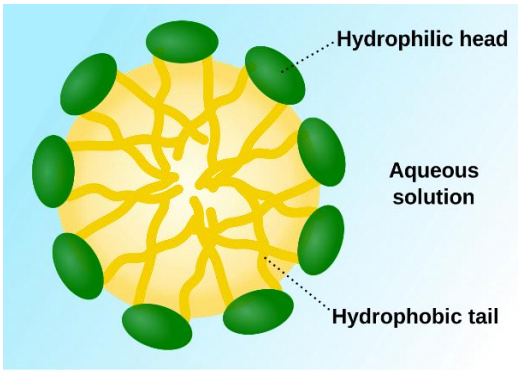

Figure 4 *– Schematic of a micelle formed by phospholipids in an aqueous solution [18].*

Surfactants are widely used in the chemical industry, particularly as the active ingredient in soap in order to allow oils normally insoluble in water to be dissolved in the aqueous phase and easily removed. Solid particles, which will now be discussed, have distinct benefits over surfactants in creating emulsions, however. These include the ability to create both oil-in-water (o/w, oil droplets dispersed in aqueous water) and water-in-oil (w/o, water droplets dispersed in aqueous oil) emulsions with the same particles simply by adjusting the volume fraction of water, whereas surfactant systems do not invert but form gel emulsions [19]. Additionally, particle emulsions are most stable near inversion conditions, unlike surfactant emulsions which are often unstable under such conditions [19]. Another advantage of using particles is that recovery of the dispersed substance is often considerably easier than with surfactants [20]. Recovery is crucial when dealing with biologically active materials [21] or ecologically hazardous mining fluids [22].

Solid particles form emulsions when the wettability of the two liquid phases on the solid is such that the solid particles tend to adsorb at the interface. This can be visualized by **Figure 5**, where the contact angle of the particle into the aqueous water phase is dictated by the wettability of each liquid toward the solid. For contact angles below 0° or above 180°, however, emulsions are not formed because particles will preferentially partition into the higher wetting phase instead of adsorbing at the interface.

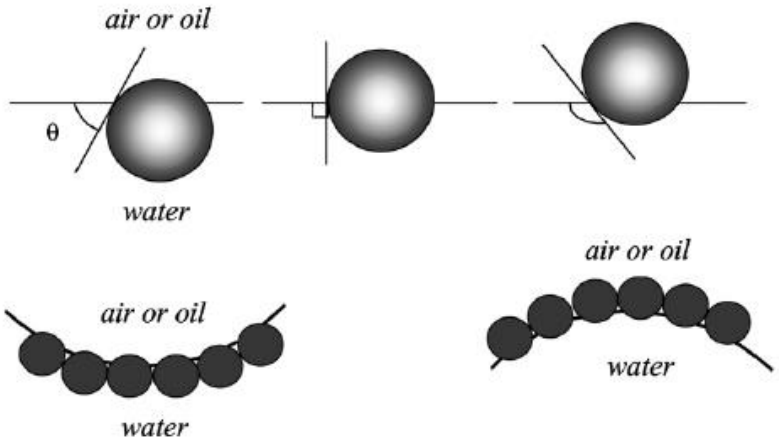

Figure 5 *– (Upper) Position of a solid particle at an oil-water interface for contact angles θ of < 90°, 90°, and > 90°. (Lower) Expected position of particles along the interface corresponding to the above contact angle.*

For contact angles less than 90°, o/w emulsions form. Likewise, w/o emulsions for contact angles greater than 90°. Typically one of these two cases is desirable in forming stable emulsions. The contact angle is controlled by the hydrophile-lipophile balance (HLB) of the particle. This is often determined by the hydrophobicity of the particles. Therefore, selecting solid particles with appropriate properties is important in achieving stable emulsions.

Once particles adsorb, the emulsion interface becomes viscoelastic, meaning it exhibits both viscous liquid behavior and solid elastic behavior. The study of these materials is called rheology As a result of this, it is generally accepted that emulsion properties are related to the viscoelastic properties of the adsorbed layer [12]. This work will focus on characterization such interfaces in order to obtain a better understanding of their behavior and potential applications.

3.3 Objectives

As mentioned earlier, CNT-stabilized emulsions have potential to impact a variety of fields. Currently, the field of nanoparticle monolayers, particularly those with high aspect ratios such as CNTs, has been largely unexplored [23]. Study of the microstructure and rheology of CNTs at air-water interfaces then has two objectives: 1) to investigate potential applications of CNTs in create stable emulsions, 2) to understand the behavior of particles with nanoscale dimensions and high aspect ratios as they relate to micron-sized spherical particles, which have been more extensively studied.

In order to accomplish these objectives, a number of characterization techniques were utilized. First, CNT lengths were measured to determine aspect ratio quantitatively. Surface pressure and microstructure of both untreated, non-functionalized (nf) CNTs as well as CNTs functionalized with carboxyl groups were investigated via continuous compression experiments. The compression and shear moduli and viscosities were studied using oscillatory compression with a dual-balance Langmuir trough. The non-linear regime was explored by large amplitude oscillatory compression (LAOC) tests with comparison to large amplitude oscillatory shear (LAOS) tests.

4. Experimental Methods

4.1 Materials

Multiwalled CNTs produced via chemical vapor deposition (CVD) from Sigma-Aldrich (Cat# 659258, Lot# MKBG9911V) were used. The diameter is approximately 110 nm and they have about 40 layers. The untreated material is henceforth referred to as nf-CNTs. Carboxyl-functionalized carbon nanotubes (f-CNTs) were prepared by sonication in a mixture of 3:1 sulfuric acid (98%, Fisher Scientific) and nitric acid (70%, Sigma Aldrich) at 50 °C in a bath Branson sonicator. The f-CNTs were removed from the mixture by vacuum filtration with a 10 μm polytetrafluoroethylene (PTFE) membrane (Millipore). The filtered CNTs were washed with water and freeze-dried at -25 °C (Labconco FreeZone) for 72 hours.

4.2 CNT Length Characterization and Contact Angle

The effect of sonication time on length was studied by preparing samples of nf-CNTs and f-CNTs dispersed in chloroform. The nf-CNT samples were sonicated for 0 hours and 2 hours. The f-CNT samples were further sonicated for 0, 0.5, 2, and 8 hours to determine whether additional defects had been introduced by functionalization which could have impact length. For the 0 hour sonication samples, dry powders were dispersed in chloroform briefly by bath sonication (Branson). The other samples were sonicated with a tip sonicator (Branson 450 Digital Sonifier; 20% amplitude). The dispersions were then dried, resuspended in water, and deposited onto a glass slide through water evaporation. A thin layer (3-5 nm) of gold and palladium was sputtered onto the surface to allow for conduction during SEM. The images were then analyzed using ImageJ.

Accurately measuring the contact angle at the air-water interface is a challenge for sub-micron particles, as individual particles are not easily resolvable at the interface [23]. In order to measure the contact angle, a gel trapping method was used [24]. A 2 weight % solution of gellan gum (Sigma-Aldrich, Cat. No. P819169, Lot No. 011M0119 V) was mixed and heated to 95 °C. The solution was transferred to a beaker and maintained at 50 °C on a hot plate. The CNTs were spread on the interface, and the solution was cooled to room temperature in an ice bath. The beaker was left covered for 30 minutes to allow the gel to set. Polydimethylsiloxane (PDMS) elastomer (Sylgard 184) was prepared in a 10:1 ratio by mixing with a curing agent, then degassed in the centrifuge at 2000 RPM. The elastomer was then poured over the gelled water and left to cure for 48 hours. The elastomer was then peeled off the surface and washed in water bath at 95 °C for 2 minutes to remove remaining gellan. Atomic force microscopy (AFM) was used instead of scanning electron microscopy (SEM) because the latter requires sputtering a thin layer of conductive material onto the elastomer to prevent charging, which could significantly affect the measurement of the contact angle given the small diameter of the CNTs (c.a. 110 nm). AFM was performed in tapping mode (Asylum Research MFP-3D AFM with an integrated Nikon TE-2000 inverted optical microscope, Santa Barbara, Sunnyvale, CA). Silicon nitride (Si_3N_4) probes (Microlever, Park Science Instruments, Sunnyvale, CA) were used with a pyramidal tip (radius of curvature: ~50 nm) and a nominal spring constant of ~0.06 N/m. The lever spring constant was calibrated by the thermal noise method. The position of CNTs at the interface was then estimated from the height measured in the AFM images.

4.3 Spreading Protocol

Spreading dispersions were prepared by dispersing 2 mg of CNT dry powers in 10 mL of chloroform (0.2 mg/mL concentration) via tip sonication for 2 hours (Branson 450 Digital Sonifier; 20% amplitude). Chloroform was used because of its immiscibility with water and ability to

disperse CNTs. A calibration curve for the actual concentration of the supernatant was created by preparing dilutions of known volume and measuring the absorbance at a wavelength of 500 nm (Shimadzu, UVmini-1240 UV-vis spectrophotometer). The diluted dispersions were then filtered through a 250 nm Teflon membrane. The membrane was dried for 12 hours at 80 °C and weighed. From the weight difference of the membrane and the known volume, the supernatant concentration was calculated. It was found to follow Beer-Lambert's law at low absorbance values.

A Langmuir trough (KN 3005 Langmuir-Pockels trough) was used to for establishing the interface. The trough width was 146.7 mm and the minimum compression area was 23 cm^2. Approximately 150 mL of deionized water produced by a Millipore (Milli-Q) with resistivity > 18 MΩ was added to the trough to form the air-water interface. The interface was compressed to the minimum area by Derlin barriers and the surface pressure was measured using a platinum Wilhelmy plate oriented parallel to the barriers attached to a microbalance. If the surface pressure exceeded 0.3 mN/m, the interface was aspirated and compressed again to check for contamination.

The CNT dispersion was then added dropwise onto the interface suing a 500-μL syringe over the course of 3 hours until the desired coverage was reached. The dispersions were added slowly to allow chloroform to evaporate before large drops could form and sink to the bottom of the trough.

4.4 Continuous Compression Experiments

The interface was loaded with 0.6624 mg of CNTs (either f or nf). The trough was compressed from 243 (completely open) to 23 cm^2 and then expanded again. This was repeated until 5 compression/expansion cycles had been performed. Multiple trials were performed where surface pressure was measured with a Wilhelmy plate to confirm reproducibility. The plate was then removed and the trough was mounted on an upright bright-field optical microscope (Olympus BZ50; 5× magnification objective). Video was recorded at 2 frames per second (iDS UI-3360CP-C-HQ) during compression/expansion cycles to study the microstructure in situ. Langmuir-Schaefer deposition was also used to prepare thin films for SEM. A 20 × 20 mm glass coverslip was held horizontally above the interface using a suction cup. The glass substrate was lowered at a speed of 5 mm/min until contact was made with the interface. The substrate was removed from the interface at the same speed and the water was removed by trying at 75 °C for 12 hours. The substrate was prepared for SEM in a similar manner as for length characterization in order to allow resolution of individual CNTs, which is beyond the diffraction limit of optical microscopy.

4.5 Dual Balance Experiments

The interfacial stress in a Langmuir trough is a combination of compression and shear because the compression is uniaxial. Developments have suggested that these stresses can be measured using two Wilhelmy plates positioned parallel and perpendicular to the barriers [25] [26]. In order to study this relationship for CNT-laden interfaces, a second microbalance was added and the platinum Wilhelmy plates were replaced with paper plates. Following the previously mentioned approaches, one was oriented parallel to the balances and another perpendicular. Only nf-CNTs were used in these experiments. It is hypothesized later in this work that the f-CNTs complicate the determination of viscoelastic properties because the CNTs become negatively charged and then have electro-potential interactions when functionalized, and so there are not used henceforth. The spreading method of dispersions is identical, although additional aspiration of the interface is generally required because the paper plates have a tendency to release a surface active material upon exposure to the water.

Continuous compression experiments were performed identically as before, but the barrier

speeds were increased to 9.33 cm/min and 33.33 cm/min in order to study non-equilibrium properties. Step compression experiments were performed wherein the interface was quickly compressed at 33.33 cm/min to a target surface pressure. Compression was the halted and the interface was allowed to relax for 20-30 minutes or until the surface pressure was seen to plateau. This was repeated until 5 step compressions and relaxations had been observed. Lastly, oscillatory barrier tests were performed at a strain amplitude of 2% and compressional frequencies of 16.7, 50 and 100 mHz. The various frequencies were not tested at the same surface pressure however. Rather, one experiment was performed where, using the same strain amplitude, the interface was partially compressed and then allowed to oscillate at 16.7 mHz. It was then further compressed and allowed to oscillate at 50 mHz and then again at 100 mHz. It was observed that after partial compression, the surface pressure decayed significantly over time as the interface relaxed. This was addressed by allowing the signal to equilibrate to steady state before gathering data for analysis. This could have significantly impact the data, however, because even under small compression such as the oscillations performed, the interface could relax upon expansion. This is particularly evident at lower amplitudes and frequencies, where the barriers move slowly and allow the interface a long time to relax. This is particularly a concern at lower surface pressures, where there are larger areas of unordered domains to which the interface can relax, as will be seen in the results of the step compression tests.

4.6 Large Amplitude Oscillatory Compression (LAOC) Tests

Nonlinear oscillatory shear tests have become more common recently [27].Studies of the surface dilatational modulus are generally limited to low amplitude linear regimes, however, even though emulsions are often they are often exposed to high deformation rates during processing and production [28]. Therefore, knowledge of the response in non-linear regimes is often essential to a full understanding of these materials. Oscillatory compression tests are performed similarly as in the dual balance experiments, but with only a single platinum Wilhelmy plate parallel to the barriers. Strain amplitude was varied from 1.0 to 4.0 % and compressional frequencies of 16.7, 30, and 50 mHz were tested. Interfacial relaxation was a significant concern for the experiments using 1% strain amplitude, where the barriers expanded very slowly.

5. Experimental Results and Discussion

5.1 CNT Aspect Ratio and Contact Angle

The aspect ratio of the particles forming the monolayer is important because at sufficiently high values, capillary interactions become significant [23]. Selectively controlled aspect ratios could lead to interest experiments on the relation between capillary forces and interfacial microstructure. Functionalization and sonication of CNTs were identified as parts of the procedure that could have affected length. If defects were present in the original sample, the CNTs could have been "chopped" given sufficient force from the sonicator. Additionally, functionalization could have weakened the CNTs at these defects. Because of this, nf-CNTs were studied in their untreated form (brief bath sonication only) and after typical treatment in preparation for Langmuir trough experimentation (2 hours tip sonication). Additionally, the f-CNTs were studied for longer sonication times to investigate if functionalization impacted the defects.

Because a different number of CNTs were measured in ImageJ for each sonication time, the values across each data set were normalized so that the total number of CNTs measured in each were the same. This allowed the results shown in **Figure 6** and **Figure 7** to be interpreted more easily. The statistical data including the polydispersity index (PDI) in terms of length as defined

by Equation 2 is shown in **Table 1**. A moderate decrease in length is observed for nf-CNTs after 2 hours sonication, as indicated by the lower mean value and higher count of sonicated CNTs at lower length bins. The range of lengths was very wide, however, so the associated standard deviation is relatively large, so definite conclusions are difficult. The f-CNTs followed a similar trend, although little change was observed between 0 and 0.5 hours sonication and between 2 and 8 hours sonication. This increase in mean length from 2 to 8 hours sonication also suggests the experimental method is subject high amounts of error. With regards to PDI, the nf-CNTs were shown to have a considerably wider distribution than the f-CNTs. This could be due to the functionalization introducing additional defects and breaking existing ones more uniformly.

$$PDI = \frac{L_w}{L_n}; L_w = \frac{\sum_i N_i L_i^2}{\sum_i N_i L_i}, L_n = \frac{\sum_i N_i L_i}{\sum_i N_i} \quad (2)$$

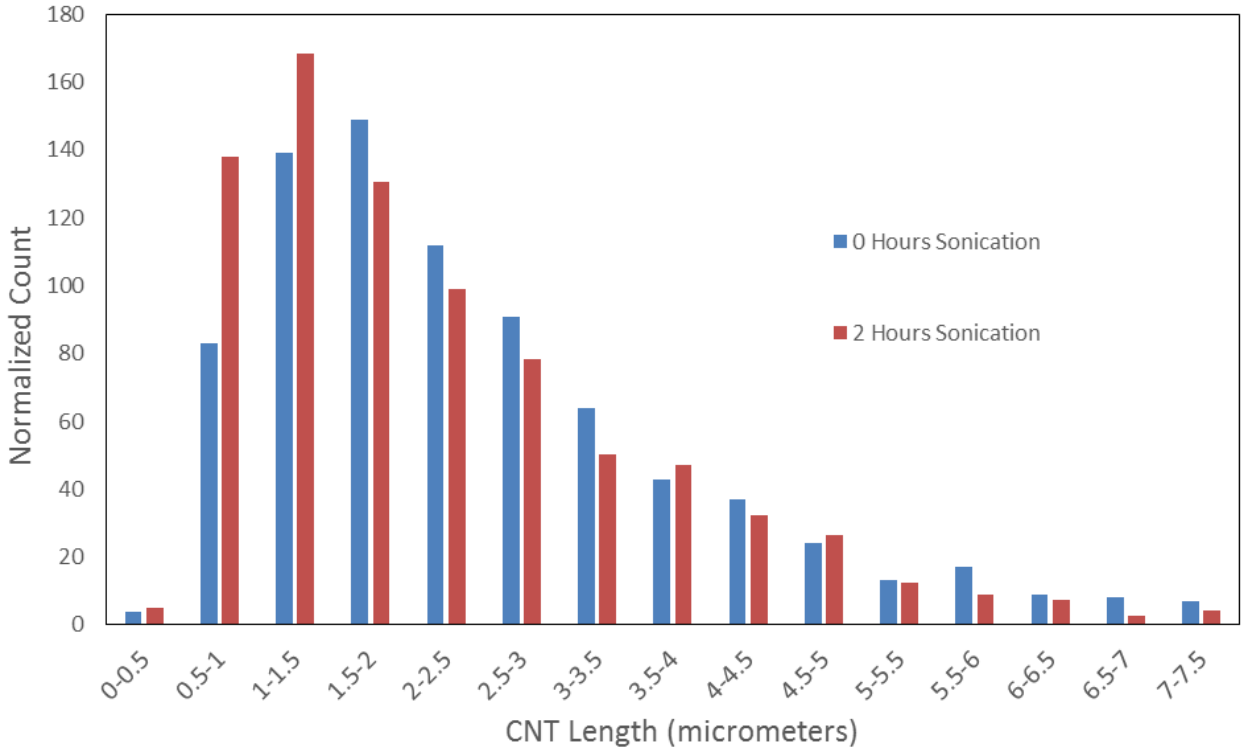

Figure 6 *– Histogram of count vs. length for nf-CNTs after 0 hours and 2 hours sonication*

Table 1 *– Statistical data corresponding to length distributions for nf-CNTs (rows 1-2) and f-CNTs (rows 3-6)*

Data Set	*Count*	*Mean Length (μm)*	*Stand Dev (μm)*	*PDI*
nf-0 h	818	2.59	1.75	2.11
nf-2 h	918	1.98	1.04	1.70
f-0 h	938	2.98	1.49	1.24
f-0.5 h	1568	2.97	1.50	1.25
f-2 h	1116	2.60	1.36	1.26
f-8 h	1648	2.68	1.41	1.26

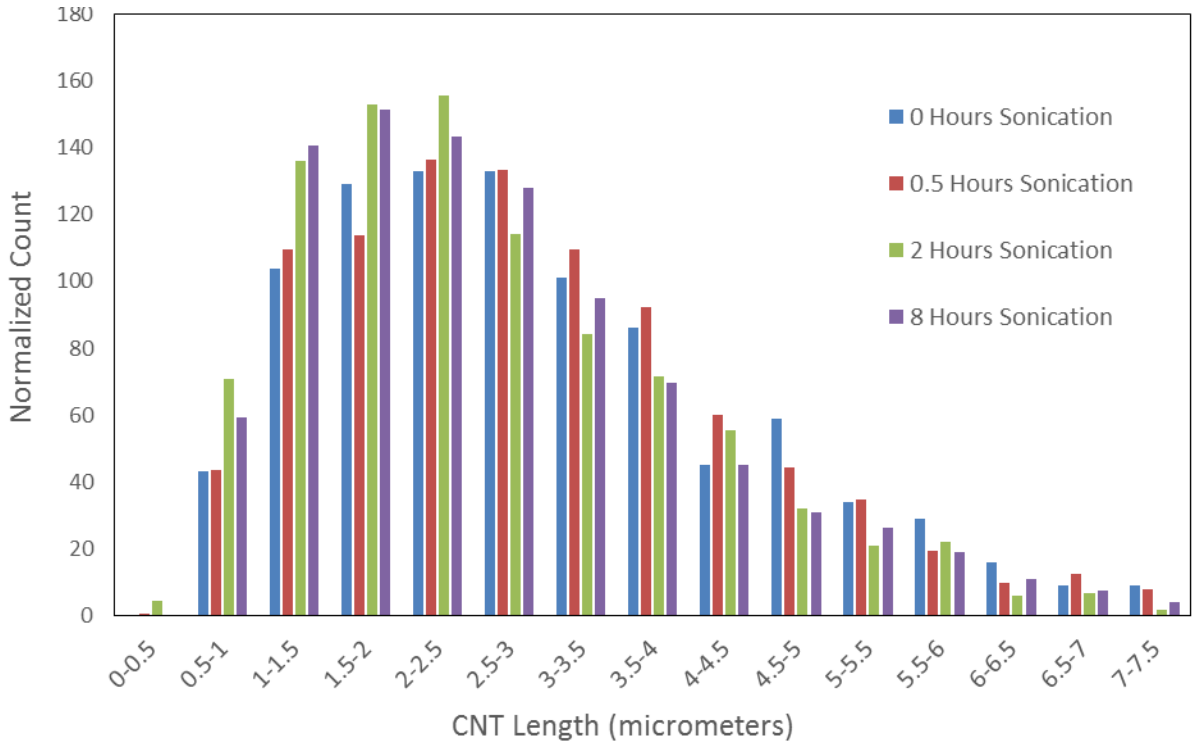

Figure 7 *– Histogram of count vs. length for f-CNTs after 0, 0.5, 2, and 8 hours sonication*

These results confirm suspected trends in length distribution. They suggest an aspect ratio of 18-24 for nf-CNTs and 24-27 for f-CNTs depending on sonication time. It was observed while measuring length that the diameter of the CNTs varies considerably, and so these values are likely wider than reported here. Due to the wide distribution, however, this technique is not suitable for producing CNTs of specific aspect ratios. As such, aspect ratio is not a focus of this work moving forward, except to comment qualitatively on capillary contributions towards intermolecular forces and their effect on the microstructure.

The contact angles measured by the gel trapping technique are 135° and 80° into the water phase for nf-CNTs and f-CNTs respectively, as seen in **Figure 8**. This is supported by previous studies, which suggest that although graphitic materials are intrinsically hydrophilic, their high surface energies cause them to adsorb at the interface and thus appear hydrophobic [29] [30]. Negatively charged f-CNTs were seen to be hydrophilic due to interactions between water and carboxyl groups. This should lead to lower surface coverage and interfacial tension and higher surface pressure. Due to electro-static interactions between CNTs, however, this is not observed, as will be discussed in the next section.

5.2 Microstructure and Surface Pressure

The surface tension of a particle-laden interface is an essential property in determining the stability of emulsions. As such, measuring it as a function of common process variables (e.g. compressional area and the related strain rate and amplitude) has become commonplace [23]. Shear rheometers are sometimes used characterize interfacial viscoelasticity and microstructure, but in preliminary experiments, data measured with a du Noüy ring geometry were inconclusive. Surface pressure measurements with a Langmuir trough were easier to interpret, and therefore were used as the primary technique in this work.

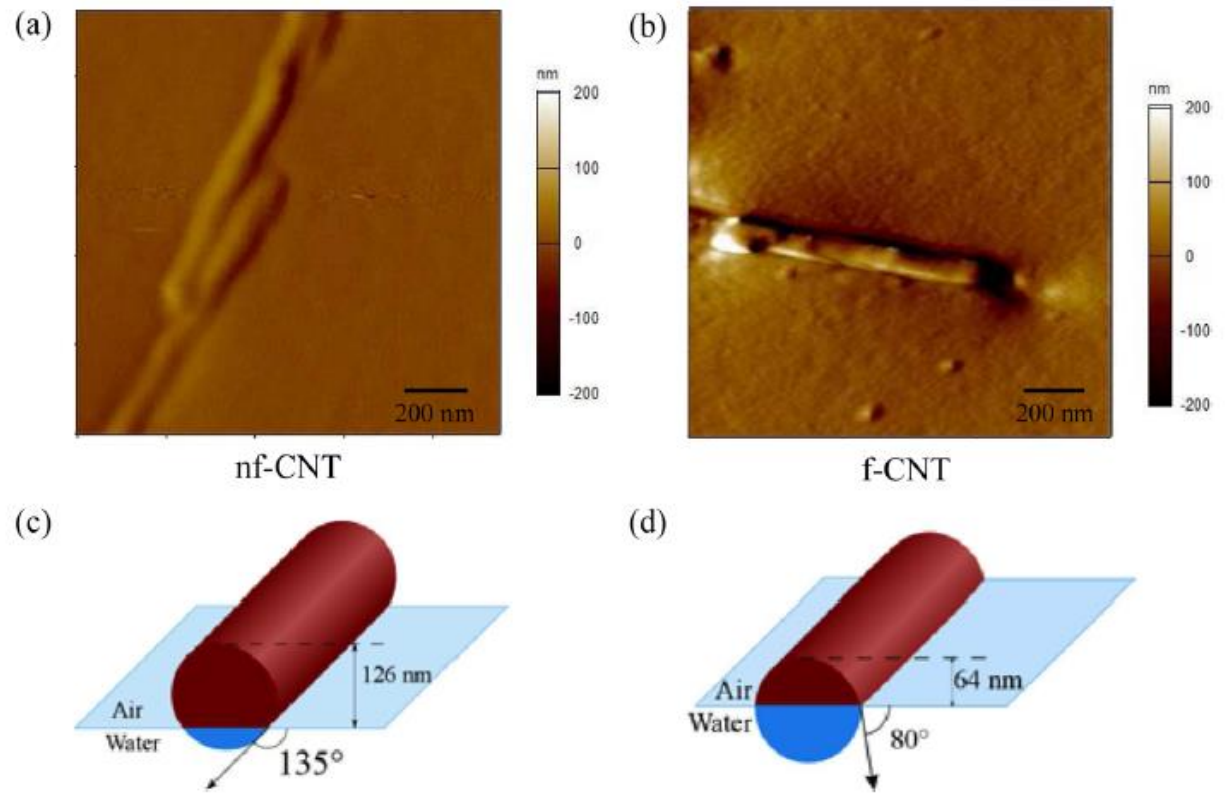

Figure 8 *– AFM images of (a) nf-CNT and (b) f-CNT in PDMS as prepared by the gel trapping technique (c) nf-CNT and (d) are schematic diagrams showing the projected positions at the air-water interface. Reproduced from publication authored by graduate mentor Sahil Vora [31].*

Considering nf-CNTs first, the apparent surface pressure Π as a function of compressional area is shown in **Figure 9**. It is called apparent because recent studies have Wilhelmy plates measure both thermodynamic and mechanical contributions [32]. The inset displays compressional elastic modulus K defined by Equation 3 as a function of surface pressure.

$$K = -A\frac{\partial \Pi}{\partial A} \tag{3}$$

Upon first compression, the surface pressure increases starting at 130 cm^2 and reaches a maximum of 63 mN/m at an area of 23 cm^2. Successive compressions percolate at smaller areas. Additionally, lower surface pressure is lower for later compressions, with the most notable drop being from the first to the second. It has been shown that spreading method and choice of dispersant can cause the first compression to differ, but not as significantly as observed here [33]. Afterwards, the water phase absorbance was tested at 500 nm to check for the presence of desorbed particles, but none were observed. Therefore, the trough was mounted on an optical microscope to study this observation in situ. It was seen that black "islands" appeared at the interface after sufficient compression, whereas a typical monolayer of would be expected to appear more uniformly grey like the networks seen at other areas in the trough. This suggested that as CNTs rearranged into more ordered networks during compression, 3D aggregates were formed. Because optical microscopy cannot resolve individual CNTs, part of the interface was deposited onto a glass

substrate and observed with SEM. This seemed to confirm the presence of 3D aggregates, as shown in **Figure 10**, although the deposition process could have altered the interface, so this cannot be certain.

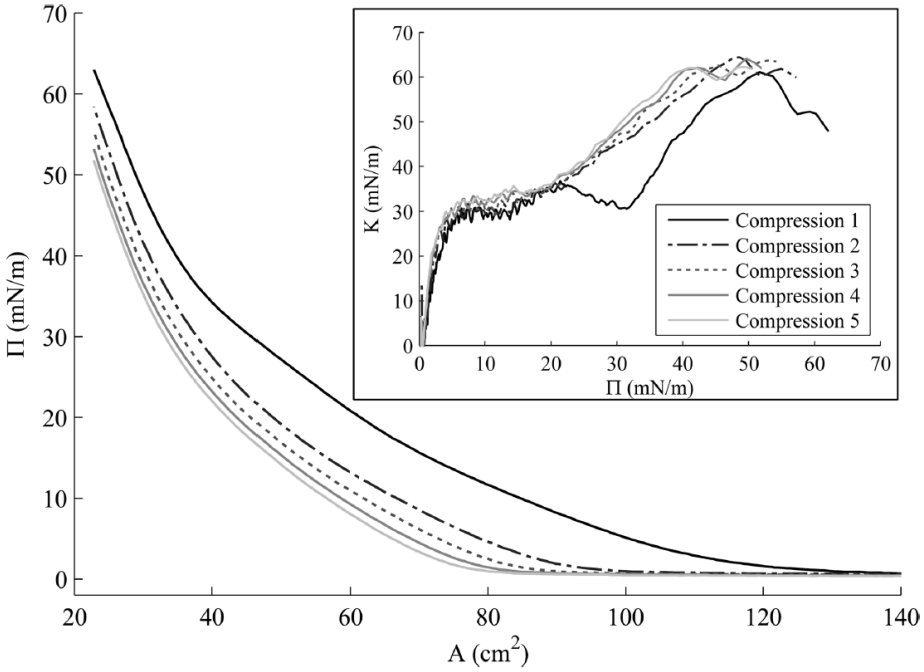

Figure 9 *– Apparent surface pressure-compression area isotherm of nf-CNTs for five successive compression cycles at a compression speed of 5 mm/min. Inset: Compressional elastic modulus as a function of apparent surface pressure. Figure reproduced from publication authored by graduate mentor Sahil Vora [31].*

Moving forward on the assumption that 3D aggregates are formed, the delayed percolation and decrease in maximum surface pressure are explained by the decreased surface coverage at the interface. Additionally, this explains differences in the compressional elastic modulus between cycles. The initial rise is associated with the contact of CNT "islands". The following plateau could be a result of rotation of these networks under compressional stress. Modulus then continues to increase as the networks cannot achieve a more ordered state by rotation. This could also explain why the second increase is delayed on the first compression, as the CNTs would be most disordered and therefore have more opportunity to rotate.

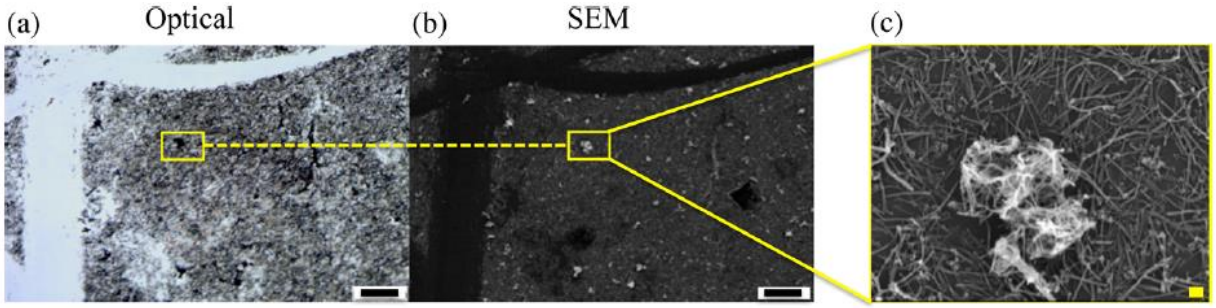

Figure 10 *– nf-CNT layer transferred onto a glass slide by Langmuir-Schaefer deposition. (a) Optical microscopy identifying a potential 3D aggregate (b-c) SEM enhancement of this region,*

resolving individual CNTs and showing 3D aggregation. Scale bars: 50 μm in panels a and b; 1 μm in panel c. Reproduced from publication authored by graduate mentor Sahil Vora [31].

Moving onto f-CNTs, **Figure 11** shows the first compression isotherm for nf-CNTs and f-CNTs overlaid. The spreading solutions were well calibrated such the CNT loading at the interface was the same in both trials. The f-CNT loaded interface percolated at lower compressional areas and reached a higher maximum surface pressure. This suggests that the f-CNT interface network was more densely packed. The 3D aggregates observed at the nf-CNT interface cannot realign or rotate in order to form more dense networks, so reduced aggregation leads to a more ordered interface and lower surface pressure. Additionally, towards the end of compression the f-CNT surface pressure surpassed that of nf-CNTs because 3D aggregation was less likely. Aggregation increases at high surface pressures near collapse pressure when the domains cannot rotate. This was investigated again by optical microscopy. **Figure 12** shows for the same compression area, the f-CNTs formed more densely packed networks and experienced less 3D aggregation, as evidenced by the darker grey fractal areas and the reduction in black areas where it is hypothesized that aggregation occurs. The reduction of aggregates and increase in ordered domains is further evidenced by the compression elastic modulus, which shows less plateauing for f-CNTs and no decrease after initial percolation. This suggests CNTs continued to rearrange unhindered by 3D aggregates throughout compression until monolayer collapse was approached.

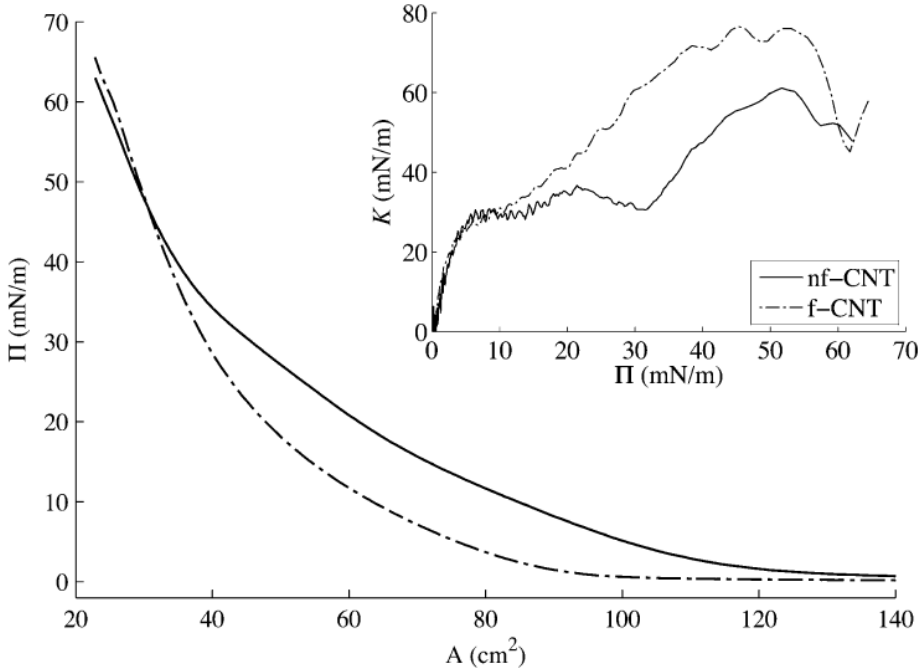

Figure 11 *– Apparent surface pressure-compression area isotherms for the first compression cycle of nf-CNT and f-CNT. The inset figure shows the compressional elastic modulus as a function of the apparent surface pressure. Reproduced from publication authored by graduate mentor Sahil Vora [31].*

The contact angle measurement earlier suggested that surface coverage should be lower for f-CNTs because they reside more in the water phase, would should have caused lower surface pressures. This was true during the first compression until maximum compression. This could have occurred due to electrostatic repulsions between f-CNT particles at higher pressures. If proximity was not hindered as in the nf-CNT case, surface pressure might have been lower throughout. The

lower contact angle also suggests the delayed percolation could have been caused by caused by lower surface coverage, not a reduction in aggregation. Inspection via optical microscopy such as in **Figure 12** consistently showed more ordered networks and fewer black "islands", which seems in line with the earlier explanation. The cause of the differences in microstructure and surface pressure and therefore somewhat speculative at this point, but this author's interpretation is that the electrostatic interactions of f-CNTs lead to more ordered interfacial networks because of reduced 3D aggregation.

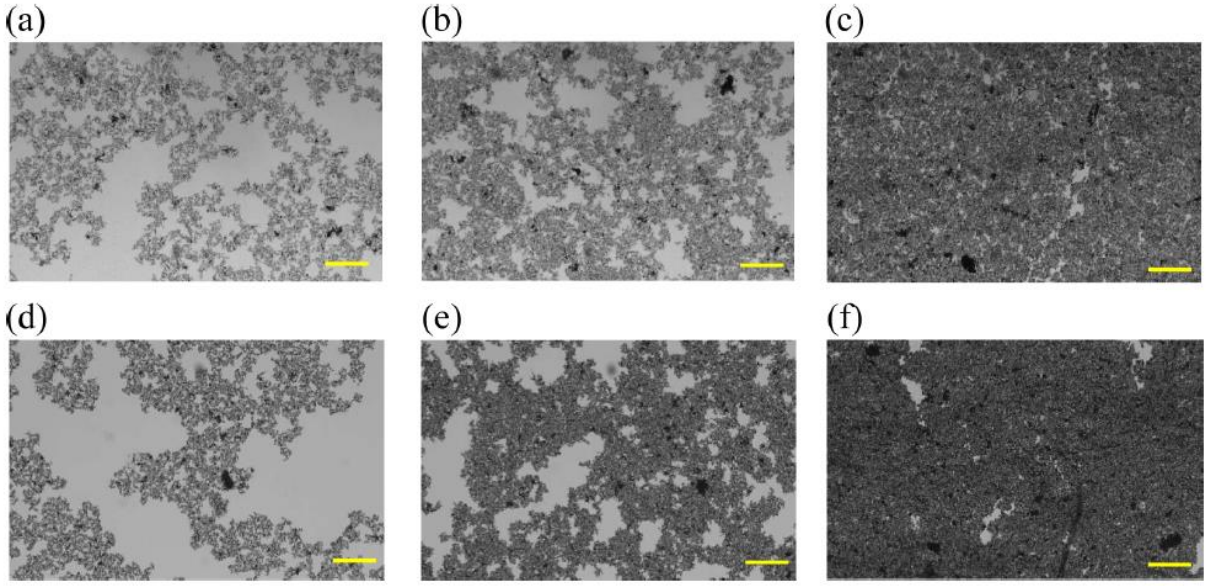

Figure 12 *– (a-c) Optical micrographs during the first compression of nf-CNTs at trough areas of 132 cm^2, 72 cm^2, and 25 cm^2 respectively (d-f) Show the same for compression of f-CNTs. Scale bar equals 100 μm. Reproduced from publication authored by graduate mentor Sahil Vora [31].*

5.3 Interfacial Viscoelastic Behavior

Viscoelastic behavior at the interface has commonly controlling the stability and response of adsorbed particle layers [12]. The compression in a Langmuir trough is uniaxial such that stress is a combination of compression and shear. Measuring these properties using is challenging, however, because the shear stress is relative small compared to compression. Through the use of two Wilhelmy plates for surface pressure measurements, the following equations have been derived [25]. It should be noted that two paper plates were used in place of platinum here due to availability. This causes an increase in mechanical contribution towards surface pressure because of capillary action and water uptake.

$$\Pi_{\parallel}(t) - \Pi(t=0) = (E+G)\beta(t) + (\eta_d + \eta_s)\, d\beta(t)/dt \quad (4)$$

$$\Pi_{\perp}(t) - \Pi(t=0) = (E-G)\beta(t) + (\eta_d - \eta_s)\, d\beta(t)/dt \quad (5)$$

Where E and G are the compression and shear surface elastic moduli respectively, and η_d and η_s are the compression and surface viscosities respectively. The relative compression β is defined by Equation 6. In the most general case, all variables are time dependent.

$$\beta = \ln\left(\frac{A(t)}{A(t=0)}\right) \approx u = \frac{\delta A(t)}{A(t)} \tag{6}$$

It will be shown in this section that surface pressure is time dependent due to relaxation of the interface towards an equilibrium state. Following compression by the barriers, the interface will rearrange into a lower energy state which was unachievable while being strained. This results in a decrease in surface pressure. This should occur as soon as compression begins, but it is speculated that if compression occurs rapidly enough, the relaxation time could be too long to have an impact. To study this, continuous compression experiments were performed at barrier speed of 9.33 and 33.33 mm/min. Assuming the variables are not time dependent, Equations 4 and 5 reduce to the following:

$$E = -1/2\, A\left(\frac{\delta \Pi_{\parallel}}{\delta A} + \frac{\delta \Pi_{\perp}}{\delta A}\right) \tag{7}$$

$$G = -1/2\, A\left(\frac{\delta \Pi_{\parallel}}{\delta A} - \frac{\delta \Pi_{\perp}}{\delta A}\right) \tag{8}$$

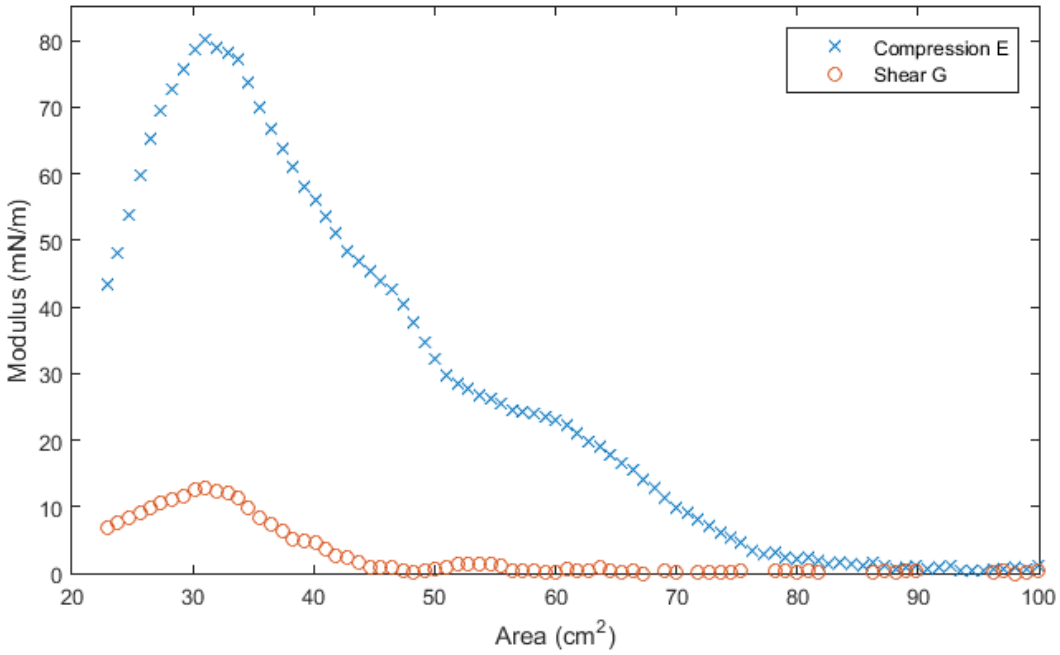

Figure 13 *– Compression and shear modulus vs. area for the fifth and final compression of a continuous compression test with barrier speed 33.33 mm/min.*

Note that modulus plots were noisy when first plotted due to vibrations in the experimentsal setup and the relatively low values being measured. Shear modulus in general, particularly during the first compression, was difficult to interpret due to few data points and low values. Because of this, the 5th and final cycle is plotted, at which point the interface is relatively stable.

Given that the interface should have more time rearrange at a lower barrier speed, it is expected that surface pressure and thus both moduli should decrease. Comparing **Figure 13** and **Figure 15**, however, it is clear that this did not occur. This is likely because CNT aggregation occurred to be

an issue, as evidence by **Figure 14**. After successive compression, the moduli were seen to increase because delayed percolation and an increase in surface pressure (as explained earlier) cause an increase in slope. The delayed uptake of E and G for the lower barrier speed suggest a similar situation as with f-CNTs, but instead of repulsion preventing the formation of 3D aggregates, it is the slower barrier speed which allows the interfacial network to realign. Because of this comments on non-equilibrium behavior and relaxation times are somewhat inconclusive, but as will be observed later, lower barrier speeds do allow for increase surface relaxation and lower surface pressures, which can appear as strain softening behavior.

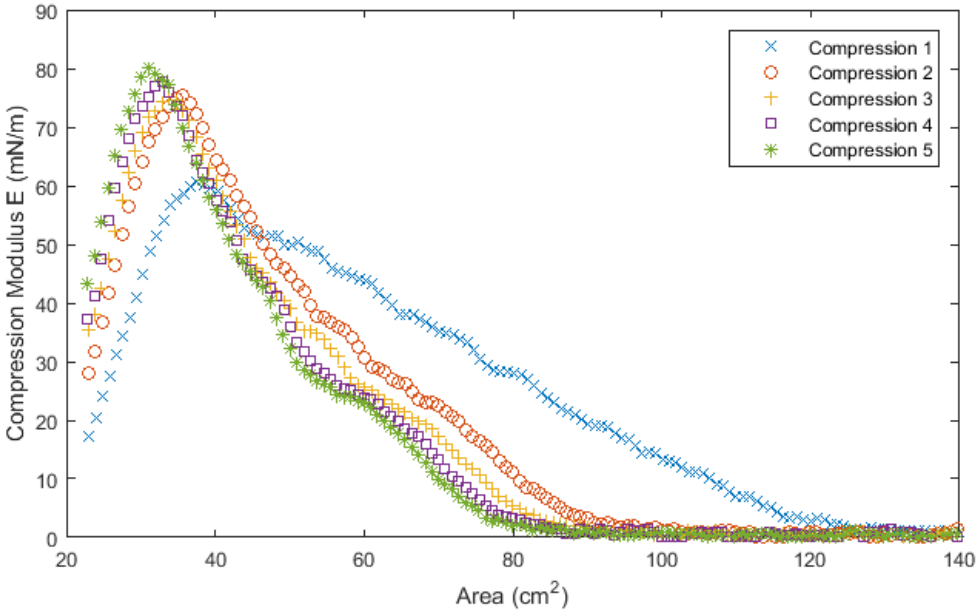

Figure 14 *– Compression modulus vs. area for all 5 compressions. Barrier speed 33.33 mm/min*

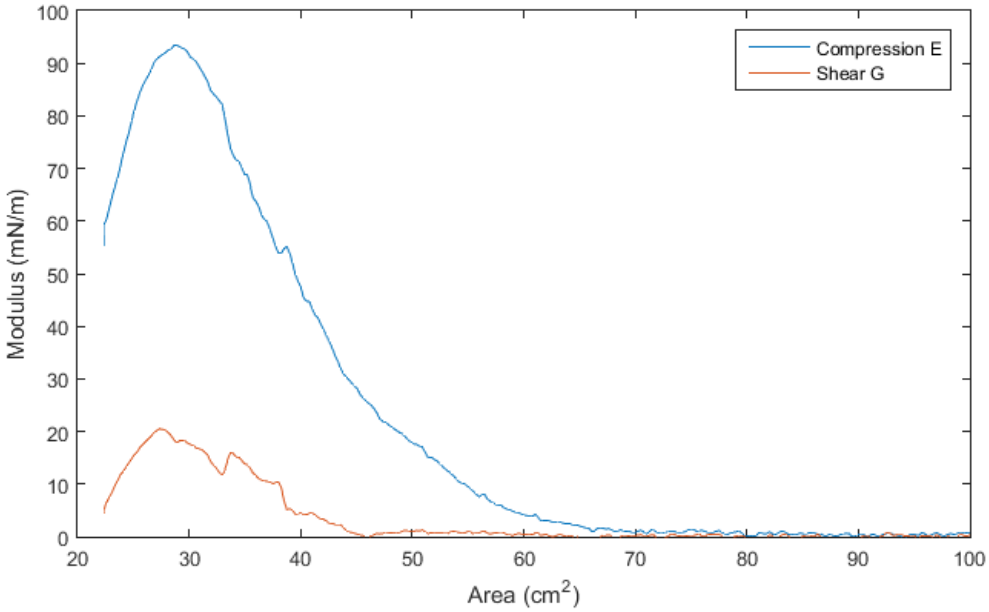

Figure 15 *– Compression and shear modulus vs. area for the fifth and final compression of a continuous compression test with barrier speed 9.33 mm/min.*

Interface relaxation was then investigated directly by a series of step compressions. **Figure 16** and **Figure 17** show the results of this experiment vs. time and compressional area respectively. The sharp decreases followed by increases in surface pressure in the latter correspond to when compression was halted for 20-30 minutes and then resumed. This shows that in the regions where compression is paused, the system variables are time dependent only. As a result, the following equation for the modulus are obtained:

$$E(t) = 1/2\left(\Pi_{\parallel}(t) + \Pi_{\perp}(t)\right) \tag{9}$$

$$G(t) = 1/2\left(\Pi_{\parallel}(t) - \Pi_{\perp}(t)\right) \tag{10}$$

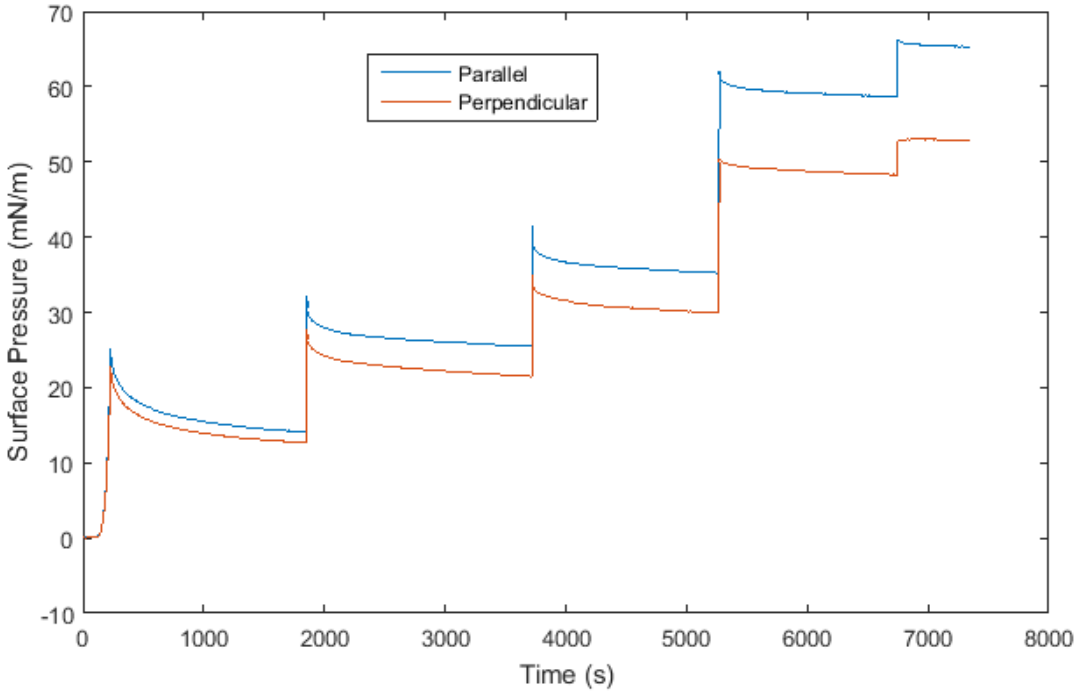

Figure 16 *– Parallel and perpendicular surface pressure vs. time for step compressions*

Figure 18 shows that the moduli decay over long periods of time. Steady state is not reached for 2-3 hours, but for the purpose of this work only shorter time relaxations are investigated. The moduli decay after each step compression can be well fit by a three term exponential, but this does not provide any particularly valuable information about the system or its behavior, and so evaluation is forgone here. The relaxation time is longer at lower surface coverage. This is intuitive because the interface has more free regions in which to rearrange. This effect has been seen in similar studies using spherical silver nanoparticles [26]. The effect of relaxation time in oscillatory experiments, especially considering mechanical contributions, will be discussed further in the following section on non-linearity.

Next, oscillatory compression where variables are time and area dependent was considered. This experiment reveals more interfacial viscoelastic information than the previous two, and is the most directly analogous to oscillatory shear rheometry, which is widely used for characterization of bulk properties and has also been used increasingly for interfacial measurements recently [27]. The area now oscillates with frequency ω, so $\delta A(t) = \delta A_0 \sin(\omega t)$, and Equations 4 and 5

become:

$$\Pi_{\parallel}(t) - \Pi(t=0) = \frac{\delta A_0}{A}[(E+G)\,sin(\omega t) + (\eta_d + \eta_s)\,cos(\omega t)] = \Pi_{0\parallel}\,sin(\omega t + \theta_{\parallel}) \qquad (11)$$

$$\Pi_{\perp}(t) - \Pi(t=0) = \frac{\delta A_0}{A}[(E-G)\,sin(\omega t) + (\eta_d - \eta_s)\,cos(\omega t)] = \Pi_{0\perp}\,sin(\omega t + \theta_{\perp}) \qquad (12)$$

Where $\Pi_{0\parallel}$ and $\Pi_{0\perp}$ are the magnitude of the parallel and perpendicular surface pressures respectively and $\theta_{\parallel}$ and $\theta_{\perp}$ are the phase angles between strain and pressure.

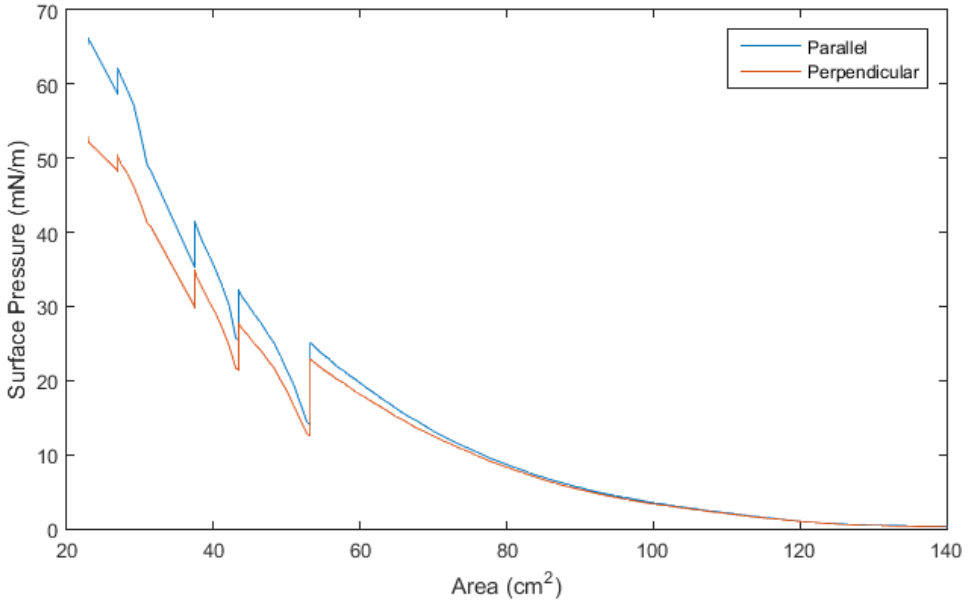

Figure 17 *– Parallel and Perpendicular surface pressure vs. area for step compressions*

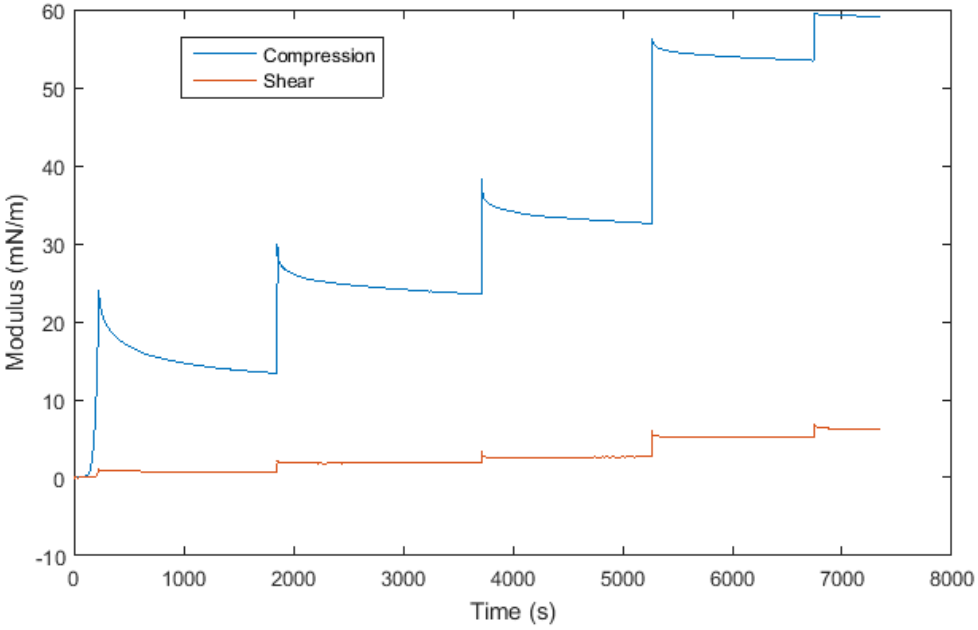

Figure 18 *– Compression and shear modulus vs. time for step compressions*

The phase angles are obtained by data treatment. The shear and compression stresses, elastic moduli, and viscosities can then be determined as follows:

$$\sigma_E = (\Pi_{0\parallel} + \Pi_{0\perp})/2u_0 \tag{13}$$

$$\sigma_G = (\Pi_{0\parallel} - \Pi_{0\perp})/2u_0 \tag{14}$$

$$\mathrm{E} = \left[\left(\Pi_{0\parallel} - \Pi(t=0)\right)\cos(\theta_\parallel) + \left(\Pi_{0\perp} - \Pi(t=0)\right)\cos(\theta_\perp)\right]/(2\mathrm{u}_0) \tag{15}$$

$$G = (\Pi_{0\parallel}\cos(\theta_\parallel) - \Pi_{0\perp}\cos(\theta_\perp))/(2u_0) \tag{16}$$

$$\omega\eta_d = \left[\left(\Pi_{0\parallel} - \Pi(t=0)\right)\sin(\theta_\parallel) + \left(\Pi_{0\perp} - \Pi(t=0)\right)\sin(\theta_\perp)\right]/(2u_0) \tag{17}$$

$$\omega\eta_s = (\Pi_{0\parallel}\sin(\theta_\parallel) - \Pi_{0\perp}\sin(\theta_\perp))/(2u_0) \tag{18}$$

Table 2 *– Viscoelastic parameters for various frequencies under oscillatory compression with 2% strain amplitude*

ω (mHz)	σ_E (mN/m)	σ_G (mN/m)	E (mN/m)	G (mN/m)	$\omega\eta_d$ (mN/m)	$\omega\eta_s$ (mN/m)
16.7	156.6	17.79	156.5	17.77	5.81	0.69
50	164.4	21.32	164.4	21.31	2.81	0.54
100	154.0	23.32	154.0	23.32	1.71	0.30

The results in **Table 2** show that compression stress is significantly higher than shear stress, which is in line with previous findings. Additionally, phase angles are small so the compression and shear modulus vary little from the stress values as predicted by Equations 13 – 16. Shear stress was seen to increase with frequency, although only slightly. Compression stress was relatively unaffected by changes in frequency. Surface viscosities were fairly low for all frequencies but were higher at lower frequencies. In order to visualize the behavior of the interface in response to strain, the surface pressures were normalized to values from -1 to 1 and plotted against strain. Such plots are referred to as Lissajous curves and more commonly have stress on the y-axis.

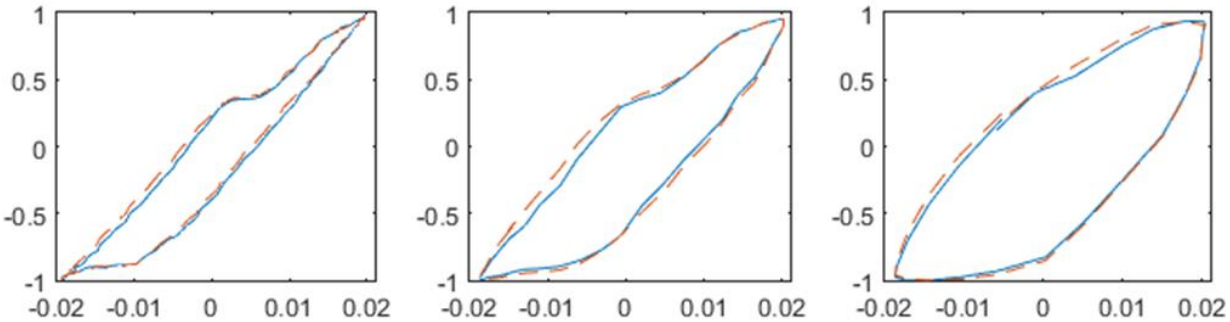

Figure 19 *– The x and y axis for each figure are Strain % and Normalized Surface Pressure respectively. The solid line and dotted lines are parallel and perpendicular surface pressure respectively. The strain amplitude is 2% for every figure. (Left) frequency = 16.7 mHz (Middle) frequency = 50 mHz (right) frequency = 100 mHz*

Figure 19 shows that at low frequencies, the behavior is nonlinear. This is evaluated by comparing the minimum compression modulus (tangent of the Lissajous curve at zero strain) and maximum compression modulus (secant modulus, evaluated at maximum compression). For interfacial shear rheometry, the linearity is generally defined by two elastic moduli because the oscillation is symmetric. Lissajous plots of surface pressure are often asymmetric, however, because compression and expansion in a Langmuir trough are not identical [28]. These plots thus have four defining moduli, two for compression and two for expansion. For frequencies of 16.7 mHz and 50 mHz at a strain amplitude of 2%, the interface is strain softening because the minimum compression modulus is greater than the maximum compression modulus. At a frequency of 100 mHz, the interface is relatively linear because the moduli are approximately equal. In order to study this effect and its causes, the experimental procedure was simplified to use only one platinum balance in a parallel orientation.

The compression modulus from the oscillatory experiments is significantly higher than for continuous and step compressions, but the shear rate was higher as well. In general, the viscoelastic parameters measured by each experiment were difficult to compare because the equation used were derived for monolayers, and this system exhibits significant deviations from the ideal monolayer. The possibility of 3D aggregations and capillary interactions due to high aspect ratio complicate the surface rheological properties to the extent the equations above deviate significantly from the true values. They are useful in comparison to microstructural observations and offering further evidence to support to idea of aggregation, however.

5.4 Oscillatory Compression Non-linearity

Although interfacial viscoelastic properties cannot be measured with a single balance, the previous section shows that stress and surface pressure are related. Therefore, a range of experiments were conducted measuring only surface pressure in order to make the experimental procedure faster and less complicated. Following a similar procedure as before but without the second balance, experiments were performed at strain amplitude of 1%, 2%, and 4%. Frequency range was adjusted to 16.7, 30, and 50 mHz.

Lissajous plots of normalized parallel surface pressure versus strain, seen in **Figure 20**, show that the surface pressure response is more linear at high frequencies and high strain amplitudes given the same frequency. This makes sense in the context of relaxation times because at low frequencies and low strain amplitudes, the barriers have a lower velocity. This allows the interface more time to rearrange, which generally results in strain softening behavior. Only the bottom row corresponding to a strain amplitude of 1% exhibits strain hardening behavior on compression.

Strain softening is explained by mechanical influence of the plate. When the interface expands or moves slowly, the CNTs gathered around the plate due to local curve and capillary forces spread out more, reducing surface pressure. Another explanation could involve aggregation of CNTs during compression, which would lower the surface pressure by reducing the surface coverage. At high frequencies and amplitudes this effect is less noticeable because the barriers move sufficiently fast that the interface does not significantly relax, and the surface pressure continues to increase.

Strain hardening at low amplitudes is more difficult to explain. It could occur because the barrier speed is so slow that the interface has already relaxed significantly on the expansion part of the cycle. The interface would then experience an increase in surface pressure as its lower energy state is disturbed by the next compression. This would be consistent with the isotherms observed for f-CNTs where there was less plateauing in the compression elastic modulus. This is speculative, however, and further experimentation is needed for a sounder hypothesis.

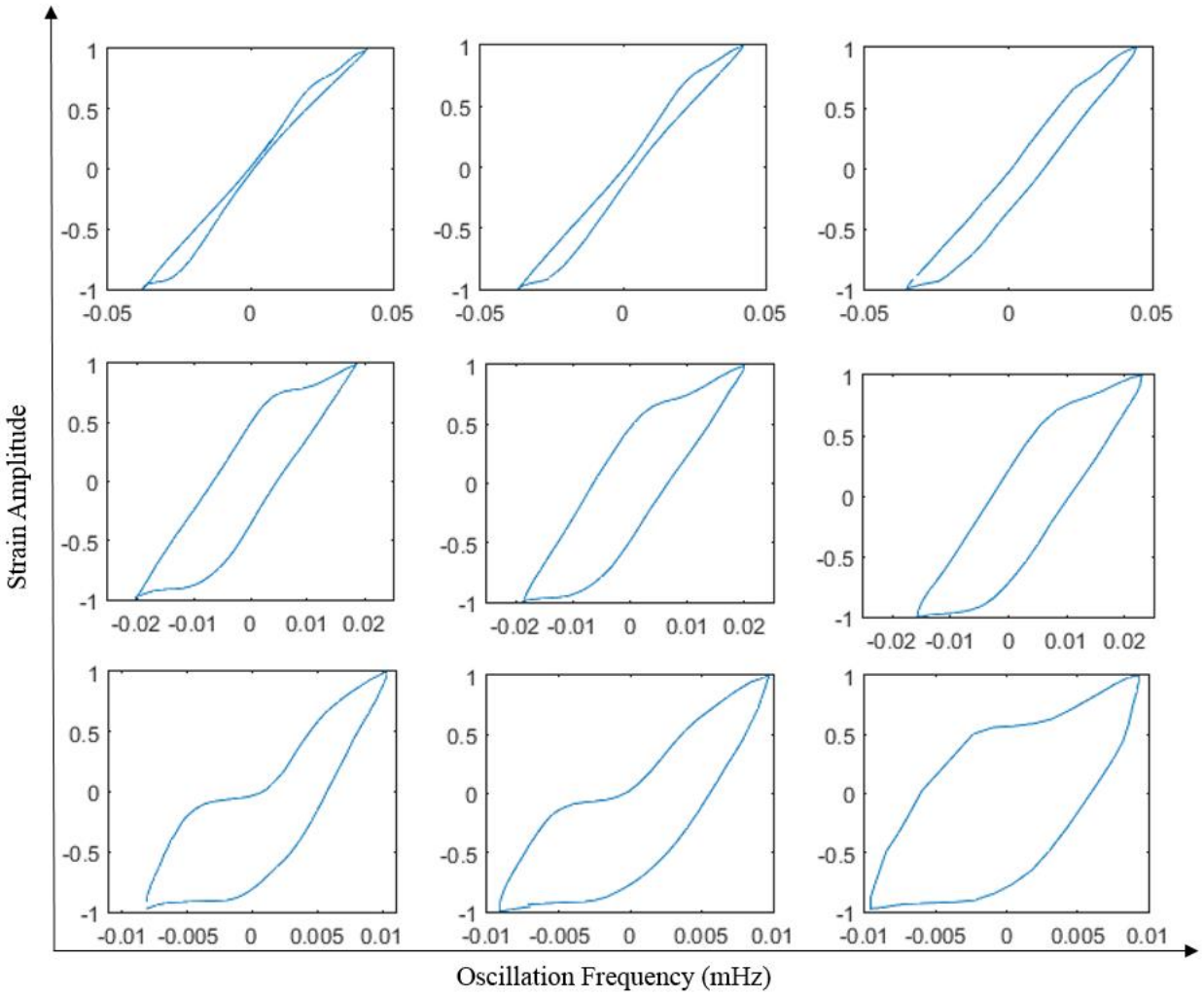

Figure 20 *– The x and y axis for each plot Strain % and Normalized Surface Pressure respectively. All plots in the left column have a frequency of 16.7 mHz and those in the middle and right have frequencies of 30 mHz and 50 mHz respectively. The bottom, middle, and top rows correspond to strain amplitudes of 1%, 2%, and 4% respectively.*

6. Conclusions

A wide variety of experimental methods and techniques were utilized to characterize both nf-CNTs and f-CNTs at air-water interfaces. Properties fundamental to interfacial science such as particle size, aspect ratio, and contact angle were investigated. The microstructure was explored through surface pressure measurements and optical microscopy. Although challenges arose when aggregation was suspected and supported by multiple experiments, adjustments were made to account for the fact that the interface was not a perfect monolayer. Differences between nf-CNT and f-CNT interfaces were analyzed, and it was determined the electrostatic repulsions between negatively charged carboxyl groups reduced aggregation in CNTs and lead to more ordered films adhering more closely to expected monolayer behavior.

Carrying forward these microstructural observations into rheological characterization of nf-CNTs, a dual balance approach was developed for calculation of compression and shear moduli. Non-steady state compression experiments as well as time-dependent step compressions were

performed to establish the idea of relaxation in the interface and when it was significant. These conclusions regarding interfacial relaxing were considered together with aggregation to explain the compression and shear elastic moduli, stresses, and viscosities in dual barrier oscillatory experiments. Different frequencies were tested, and while the rheological properties were not seen to change significantly, nonlinear behavior was observed. This prompted further investigation with a variety of amplitudes and frequencies. The results of these experiments show that the interface displayed both strain softening and strain hardening characteristics depending upon the operating conditions. Non-linear behavior was tied back to aggregation and relaxation to propose reasoning as to why the interface behaved as it did.

Overall, the results are highly intriguing and prompt the need for further study of this interface. In particular more controlled dual balance experiments could yield valuable information. Testing at a variety of shear rates and amplitudes would provide a wealth of information in more effectively characterization the interface. As was shown in this work, the existing models for monolayers can be made suitable for analysis of CNT-laden interfaces, even though they have dissimilarities.

7. References

[1] W. Ramsden, "Separation of Solids in thie Surfae-layers of Solution 3 and ' Suspensions ' (Observations on Surface-membranes, Bubbles, E.tmulsions, and Mechanical Coagulation). - Preliminary Account," *Proceedings of the Royal Society of London,* vol. 72, pp. 156-164, 1903.

[2] S. U. Pickering, "CXCVI.-Emulsions," *Journal of the Chemical Society, Transactions,* vol. 91, pp. 2001-2021, 1907.

[3] L. L. Schramm, Emulsions, foams, and suspensions: fundamentals and applications, Weinheim: John Wiley & Sons, 2005.

[4] O. D. Velev and A. M. Lenhoff, "Colloidal crystals as templates for porous materials," *Current Opinion in Colloid & Interface Science,* vol. 5, pp. 56-63, 2000.

[5] Y. Yin, B. Gates and Y. Xia, "Growth of large crystals of monodispersed spherical colloids in fluidic cells fabricated using nonphotolithographic methods," *Langmuir,* vol. 17, pp. 6344-6350, 2001.

[6] K. Y. Yoon, S. J. An, Y. Chen, J. H. Lee, S. L. Bryant and R. Ruoff, "Graphene Oxide Nanoplatelet Dispersions," *J. Colloid Interface Sci.,* vol. 403, pp. 1-6, 2013.

[7] A. J. Worthen, H. G. Bagaria, Y. Chen, S. L. Bryant and C. Huh, "Nanoparticle-Stabilized Carbon Dioxide-in-Water," *J. Colloid Interface Sci.,* vol. 391, pp. 142-151, 2013.

[8] P. Venkataraman, J. Tang, E. Frenkel, G. L. McPherson and J. He, "Attachment of a hydrophobically modified biopolymer at the oil–water interface in the treatment of oil spills," *ACS applied materials & interfaces,* vol. 5, no. 9, pp. 3572-3580, 2013.

[9] A. Gupta, M. Sender, S. Fields and G. D. Bothun, "Phase and sedimentation behavior of oil (octane) dispersions in the presence of model mineral aggregates," *Marine pollution bulletin,* vol. 87, no. 1, pp. 164-170, 2014.

[10] A. Menner, R. Verdejo, M. Shaffer and A. Bismarck, "Particle-stabilized surfactant-free medium internal phase emulsions as templates for porous nanocomposite materials: poly-pickering-foams," *Langmuir,* vol. 23, no. 5, pp. 2398-2403, 2007.

[11] W. Zhai, G. Li, P. Yu, L. Yang and L. Mao, "Silver phosphate/carbon nanotube-stabilized

pickering emulsion for highly efficient photocatalysis," *The Journal of Physical Chemistry C,* vol. 117, no. 29, pp. 15183-15191, 2013.

[12] D. Langevin, "Influence of interfacial rheology on foam and emulsion properties," *Advances in Colloid and Interface Science,* vol. 88, no. 1, pp. 209-222, 2000.

[13] P. Erni, P. Fischer, E. J. Windhab, V. Kusnezov, H. Stettin and J. Läuger, "Stress-and strain-controlled measurements of interfacial shear viscosity and viscoelasticity at liquid/liquid and gas/liquid interfaces," *Review of scientific instruments,* vol. 74, no. 11, pp. 4916-4924, 2003.

[14] B. Finio, "Measuring Surface Tensions of Water with a Penny," Science Buddies, [Online]. Available: http://www.sciencebuddies.org/science-fair-projects/project_ideas/Chem_p021.shtml#summary. [Accessed 16 April 2016].

[15] T. Young, "An essay on the cohesion of fluids," *Philosophical Transactions of the Royal Society of London,* vol. 95, pp. 65-87, 1805.

[16] J. Gills, "Contact Angle," 17 January 2006. [Online]. Available: https://en.wikipedia.org/wiki/File:Contact_angle.svg. [Accessed 16 April 2016].

[17] T. Krebs, J. Slot, C. P. G. H. Schroen, H. Hoeijmakers and R. Boom, "Emulsion compression and coalescence under enhanced gravity studied with in-situ microscopy," in *Advances in Fluid Mechanics IX*, Southhampton, WIT Press, 2012, pp. 199-210.

[18] E. Boutet, "Micelle scheme," 12 October 2007. [Online]. Available: https://en.wikipedia.org/wiki/File:Micelle_scheme-en.svg. [Accessed 16 April 2016].

[19] B. P. Binks and S. O. Lumsdon, "Catastrophic phase inversion of water-in-oil emulsions stabilised by hydrophobic silica," *Langmuir,* vol. 16, pp. 2539-2547, 2000.

[20] B. P. Binks, "Particles as surfactants—similarities and differences.," *Current Opinion in Colloid & Interface Science,* vol. 7, no. 1-2, pp. 21-41, 2002.

[21] P. Å. Albertsson, Partition of cell particles and macromolecules: separation and purification of biomolecules, cell organelles, membranes, and cells in aqueous polymer two-phase systems and their use in biochemical analysis and biotechnology, New York: Wiley, 1986.

[22] J. Newcombe, "Emulsion breaking with surfactant recovery". U.S. Patent 4,216,079, 5 August 1980.

[23] B. P. Binks, "Special issue on coilloidal particles at liquid interfaces," *Physical Chemistry Chemical Physics,* vol. 9, pp. 6298-6299, 2007.

[24] V. Paunov, "Novel Method for Determining the Three-Phase," *Langmuir,* no. 7970-7976, p. 19, 2003.

[25] J. T. Petkov, T. D. Gurkov, B. E. Campbell and R. P. & Borwankar, "Dilatational and shear elasticity of gel-like protein layers on air/water interface," *Langmuir,* vol. 16, no. 8, pp. 3703-3711, 2000.

[26] D. Y. Zang, E. Rio, D. Langevin, B. Wei and B. P. & Binks, "Viscoelastic properties of silica nanoparticle monolayers at the air-water interface," *The European Physical Journal E,* vol. 31, no. 2, pp. 125-134, 2010.

[27] K. Hyun, M. Wilhelm, C. Klein, K. Cho, J. Nam, K. Ahn, S. Lee, R. Ewoldt and G. McKinley, "A review of nonlinear oscillatory shear tests: Analysis and application of large amplitude oscillatory shear (LAOS)," *Progress in Polymer Science,* vol. 36, no. 12, pp.

1697-1753, 2011.

[28] L. M. Sagis and P. Fischer, "Nonlinear rheology of complex fluid–fluid interfaces," *Current Opinion in Colloid & Interface Science,* vol. 6, no. 520-529, p. 19, 2014.

[29] A. Kozbial, Z. Li, C. Conaway, R. McGinley, S. Dhingra, V. Vahdat, F. Zhou, B. D'Urso, H. Liu and L. Li, "Study on the surface energy of graphene by contact angle measurements," *Langmuir,* vol. 30, pp. 8598-8606, 2014.

[30] Z. Li, Y. Wang, A. Kozbial, G. Shenoy, F. Zhou, R. McGinley, P. Ireland, B. Morganstein, A. Kunkel and S. P. Surwade, "Effect of airborne contaminants on the wettability of supported graphene and graphite," *Nature Materials,* vol. 12, pp. 925-931, 2013.

[31] S. R. Vora, B. Bognet, H. S. Patanwala, F. Chinesta and A. W. K. Ma, "Surface Pressure and Microstructure of Carbon Nanotubes at an Air-Water Interface," *Langmuir,* vol. 31, pp. 4663-4672, 2015.

[32] T. Verwijlen, L. Imperiali and J. Vermant, "Separating Viscoelastic," *Advances in colloid and interface science,* vol. 206, pp. 428-436, 2014.

[33] S. L. Duncan and R. G. Larson, "Comparing Experimental and," *Biophysical Journal,* vol. 94, no. 8, pp. 2965-2986, 2008.

8. Appendices

8.1 MATLAB Files

8.1.1 Dual Balance Continuous Compression

```
function res = Cont(xlsdata,sheet)
% xlsdata is the excel in format 'Name.xlsx'
% sheet name in format 'Name'
close all
M = xlsread(xlsdata,sheet);
A = M(:,1);
SPPar0 = M(1,2);
SPPer0 = M(1,3);
SPPar = M(:,2) - SPPar0;
SPPer = M(:,3) - SPPer0;
for i = 1:length(SPPar)
    if i == 1
        EplusG(i) = -A(i)*(SPPar(i+1)-SPPar(i))/(A(i+1)-A(i));
        EminusG(i) = -A(i)*(SPPer(i+1)-SPPer(i))/(A(i+1)-A(i));
    elseif i < length(A)
        EplusG(i) = -A(i)*(SPPar(i+1)-SPPar(i-1))/(A(i+1)-A(i-1));
        EminusG(i) = -A(i)*(SPPer(i+1)-SPPer(i-1))/(A(i+1)-A(i-1));
    end
end
E = (EplusG + EminusG)/2;
G = (EplusG - EminusG)/2;
filterfreq = 5;
coeffMA = ones(1,filterfreq)/filterfreq;
Ef = filter(coeffMA,1,E);
Gf = filter(coeffMA,1,G);
fdelay = (length(coeffMA)-1)/2;
Af = A - fdelay/length(coeffMA);
figure(1)
```

```
plot(Af(1956:2197),Ef(1956:2197),'x',Af(1956:2197),Gf(1956:2197),'o')
legend('Compression E','Shear G')
xlabel('Area (cm^{2})')
ylabel('Modulus (mN/m)')
axis([20 100 0 85])
figure(2)
plot(Af(113:242),Ef(113:242),'x',Af(492:730),Ef(492:730),'o',...
    Af(980:1218),Ef(980:1218),'+',Af(1467:1706),Ef(1467:1706),'s',...
    Af(1956:2197),Ef(1956:2197),'*')
axis([20 140 0 90])
xlabel('Area (cm^{2})')
ylabel('Compression Modulus E (mN/m)')
legend('Compression 1','Compression 2','Compression 3','Compression 4',...
    'Compression 5')
figure(3)
plot(Af(113:242),Gf(113:242),'x',Af(492:730),Gf(492:730),'o',...
    Af(980:1218),Gf(980:1218),'+',Af(1467:1706),Gf(1467:1706),'s',...
    Af(1956:2197),Gf(1956:2197),'*')
axis([20 140 0 16])
xlabel('Area (cm^{2})')
ylabel('Shear Modulus G (mN/m)')
legend('Compression 1','Compression 2','Compression 3','Compression 4',...
    'Compression 5')
end
```

8.1.2 Dual Balance Step Compression

```
function res = Step(xlsdata)
% xlsdata is the excel in format 'Name.xlsx'
close all
M1 = xlsread(xlsdata,'295a');
M2 = xlsread(xlsdata,'295b');
M3 = xlsread(xlsdata,'295c');
M4 = xlsread(xlsdata,'295d');
M5 = xlsread(xlsdata,'295e');
tstart = M1(1:210,1);
t1 = tstart(end) + M1(211:end,1);
t2 = t1(end) + M2(:,1);
t3 = t2(end) + M3(:,1);
t4 = t3(end) + M4(:,1);
t5 = t4(end) + M5(:,1);
t = [tstart ; t1 ; t2 ; t3 ; t4 ; t5];
A1 = M1(:,4);
A2 = M2(:,4);
A3 = M3(:,4);
A4 = M4(:,4);
A5 = M5(:,4);
A = [A1 ; A2 ; A3 ; A4 ; A5];
SPPar1 = M1(:,5) - M1(1,5);
SPPar2 = M2(:,5) - M1(1,5);
SPPar3 = M3(:,5) - M1(1,5);
SPPar4 = M4(:,5) - M1(1,5);
SPPar5 = M5(:,5) - M1(1,5);
SPPar = [SPPar1 ; SPPar2 ; SPPar3 ; SPPar4 ; SPPar5];
SPPer1 = M1(:,6) - M1(1,6);
SPPer2 = M2(:,6) - M1(1,6);
SPPer3 = M3(:,6) - M1(1,6);
```

```
SPPer4 = M4(:,6) - M1(1,6);
SPPer5 = M5(:,6) - M1(1,6);
SPPer = [SPPer1 ; SPPer2 ; SPPer3 ; SPPer4 ; SPPer5];
E = (SPPar + SPPer)/2;
G = (SPPar - SPPer)/2;
figure(1)
plot(t,[SPPar SPPer])
xlabel('Time (s)')
ylabel('Surface Pressure (mN/m)')
legend('Parallel','Perpendicular')
figure(2)
plot(A, [SPPar SPPer])
xlabel('Area (cm^{2})')
ylabel('Surface Pressure (mN/m)')
legend('Parallel','Perpendicular')
axis([20 140 0 70])
figure(3)
plot(t,[E G])
xlabel('Time (s)')
ylabel('Modulus (mN/m)')
legend('Compression','Shear')
end
```

8.1.3 Dual Balance Oscillatory Compression

```
function [SigE,SigG,E,G,omegand,omegans] =
LBT(xlsxdata,sheet1,sheet2,frequency)
% xlsxdata is the excel sheet in the format 'Name.xlsx'
% sheet1 is the name of the first sheet where the trough begins fully open
% sheet2 is the name of the sheet on which analysis is to be performed
% Frequency is the oscillation frequency from sheet2 in mHz
close all; % Close all other figures
%% Define Constants and load data
F = frequency*1e-03; % Frequency in Hz
T = 1/F; % Period in seconds
N = xlsread(xlsxdata,sheet1); % Load data from first sheet
SPPar0 = N(1,6); % Set parallel stress zero point
SPPer0 = N(1,7); % Set perpendicular stress zero point
M = xlsread(xlsxdata,sheet2); % Load data to be analyzed
A = M(:,4); % Trough area (cm2)
%% Determine when oscillation begins
for i = 2:length(A)
    if A(i) > A(i-1)
        Amin = min(A(i:end)); % Minimum area once oscillation begins
        Amax = max(A(i:end)); % Maximum area once oscillation begins
        A = A(i:end); % Discard values before oscillation
        t = M(i:end,1); % Times starting at first oscillation (s)
        break
    end
end
Aavg = (Amax + Amin)/2; % Area midpoint ("zero point" on sine wave)
%% Separate last five cycles of data for analysis
tstep = mean(t(2:end) - t(1:end-1)); % Seconds per time measurement
steps = round(T/tstep); % Time steps per complete cycle
SPPar = M(end-5*steps:end,6) - SPPar0; % Parallel surface pressure (mN/m)
SPPer = M(end-5*steps:end,7) - SPPer0; % Perpendicular surface pressure
(mN/m)
```

```
A = M(end-5*steps:end,4); % Trough area for last 5 cycles
t = t(end-5*steps:end); % Times for last 5 cycles
Strain = (Aavg - A)/Aavg; % Sinusoidal strain applied at interface
figure(1) % Plot to observe strain and stress before data treatment
[ax,h1,h2] = plotyy(t,[SPPar SPPer],t,Strain);
set(ax(1),'xlim',[t(1) t(end)])
set(ax(2),'xlim',[t(1) t(end)])
set(ax(1),'ylim',[min(SPPer)-3 max(SPPar)+3])
set(ax(1),'ytick',linspace(min(SPPer)-3,max(SPPar)+3,5))
set(ax(2),'ylim',[min(Strain) max(Strain)])
set(ax(2),'ytick',[linspace(min(Strain),max(Strain),5)])
xlabel('Time (s)')
ylabel(ax(1),'Stress (mN/m)')
ylabel(ax(2),'Strain ()')
legend('Parallel stress','Perpendicular Stress','Strain')
%% Data analysis to determine moduli and viscosities
u0 = max(Strain) - min(Strain);  % Strain amplitude
PiPar0 = max(SPPar) - min(SPPar); % Parallel stress amplitude
PiPer0 = max(SPPer) - min(SPPer); % Perpendicular stress amplitude
SigE = (PiPar0 + PiPer0)/(2*u0); % Amplitude of the shear stress (mN/m)
SigG = (PiPar0 - PiPer0)/(2*u0); % Amplitude of the compression stress (mN/m)
NormStrain = Strain/max(Strain); % Strain normalized to ampltiude 1
AvgSPPar = (max(SPPar) + min(SPPar))/2; % Half parallel stress amplitude
AvgSPPer = (max(SPPer) + min(SPPer))/2; % Half perpendicular stress amplitude
NormSPPar = (SPPar - AvgSPPar)/(max(SPPar) - AvgSPPar); % Parallel stress
normalized to amplitude 1
NormSPPer = (SPPer - AvgSPPer)/(max(SPPer) - AvgSPPer); % Perpendicular
stress normalized to amplitude 1
figure(2) % Plot to check for phase lag visually
[ax,h1,h2] = plotyy(t,[NormSPPar NormSPPer],t,NormStrain);
set(ax(2),'ylim',[min(NormStrain) max(NormStrain)])
set(ax(2),'ytick',linspace(min(NormStrain),max(NormStrain),5))
xlabel('Time (s)')
ylabel(ax(1),'Normalized Stress ()')
ylabel(ax(2),'Normalized Strain ()')
legend('Parallel stress','Perpendicular Stress','Strain')
% Take fft of strain and stresses to find magnitude and angular components.
% Exlude the first point as a constant
strain = fft(NormStrain);
strain = strain(2:end);
sppar = fft(NormSPPar);
sppar = sppar(2:end);
spper = fft(NormSPPer);
spper = spper(2:end);
% Take the absolute value difference between the angles to determine the
% phase lag
PSPar = abs(angle(strain) - angle(sppar));
PSPer = abs(angle(strain) - angle(spper));
PSPar = PSPar*pi/180; % Convert to radians
PSPer = PSPer*pi/180; % Convert to radians
figure(3) % Plot phase lag to check for anomalies
plot(t(2:end),[PSPar PSPer])
xlabel('Time (s)')
ylabel('Phase shift (rad)')
legend('Parallel Phase Shift','Perpendicular Phase Shift')
PSParAvg = mean(PSPar); % Take the average of the phase lag
PSPerAvg = mean(PSPer);
```

```
omega = F*2*pi; % Oscillation frequency
E = (PiPar0*cos(PSParAvg) + PiPer0*cos(PSPerAvg))/(2*u0); % Compression
surface elastic modulus
omegand = (PiPar0*sin(PSParAvg) + PiPer0*sin(PSPerAvg))/(2*u0); % Compression
surface viscosity
G = (PiPar0*cos(PSParAvg) - PiPer0*cos(PSPerAvg))/(2*u0); % Shear surface
elastic modulus
omegans = (PiPar0*sin(PSParAvg) - PiPer0*sin(PSPerAvg))/(2*u0); % Shear
surface viscosity
figure(4)
plot(Strain(end-steps:end),NormSPPar(end-steps:end),Strain(end-
steps:end),NormSPPer(end-steps:end),'--')
axis([-.02 .021 -1 1])
end
```

8.1.4 Parallel Balance Oscillatory Compression

```
function res = LBTPar(xlsdata,sheet,frequency)
close all; % Close all other figures
% xlsxdata is the excel sheet in the format 'Name.xlsx'
% sheet is the name of the sheet to be analyzed
% Frequency is the oscillation frequency from sheet2 in mHz
%% Define Constants and load data
F = frequency*1e-03; % Frequency in Hz
T = 1/F; % Period in seconds
M = xlsread(xlsdata,sheet); % Load data from first sheet
SPPar0 = M(1,6); % Set parallel stress zero point
A = M(:,4); % Trough area (cm2)
%% Determine when oscillation begins
for i = 2:length(A)
    if A(i) > A(i-1)
        Amin = min(A(i:end)); % Minimum area once oscillation begins
        Amax = max(A(i:end)); % Maximum area once oscillation begins
        A = A(i:end); % Discard values before oscillation
        t = M(i:end,1); % Times starting at first oscillation (s)
        SPPar = M(i:end,6);
        break
    end
end
Aavg = (Amax + Amin)/2; % Area midpoint ("zero point" on sine wave)
%% Data filtering to smooth signal
Strain = (Aavg - A)/Aavg; % Sinusoidal strain applied at interface
tstep = mean(t(2:end) - t(1:end-1)); % Seconds per time measurement
steps = round(T/tstep); % Time steps per complete cycle
AmpSPPar = (max(SPPar(end-steps:end)) + min(SPPar(end-steps:end)))/2;
NormSPPar = (SPPar - AmpSPPar)/(max(SPPar(end-steps:end)) - AmpSPPar);
filterfreq = round(steps/20);
coeffMA = ones(1,filterfreq)/filterfreq;
avgSPPar = filter(coeffMA,1,NormSPPar);
avgStrain = filter(coeffMA,1,Strain);
fdelay = (length(coeffMA)-1)/2;
tAvg = t - fdelay/length(coeffMA);
plotstart=round(0.75*length(tAvg));
figure(1) % Check a section of both plots for accuracy of filtered signal
plot(t(plotstart:end),SPPar(plotstart:end),tAvg(plotstart:end),avgSPPar(plots
tart:end))
xlabel('Time (s)')
```

```
ylabel('Surface Pressure (mN/m)')
legend('Raw Data','Average (Delayed)')
figure(2)
plot(avgStrain(end-steps+5:end),avgSPPar(end-steps+5:end))
end
```